High Pressure Neutron Diffraction Study of Magnetic Ordering in Erbium

Matthew P. Clay[1], Raimundas Sereika[1], Maurissa K. Higgins[1], Antonio M. dos Santos[2], Jamie J. Molaison[2] & Yogesh K. Vohra[1]

[1] *Department of Physics, University of Alabama at Birmingham, Birmingham, Alabama 35294, USA*

[2]*Neutron Scattering Division, Oak Ridge National Laboratory, Oak Ridge, TN 37831, USA*

*Correspondence: ykvohra@uab.edu

ABSTRACT

We have studied magnetic ordering in polycrystalline erbium at high pressures up to 32 GPa and low temperatures down to 10 K using neutron diffraction techniques at the Spallation Neutron Source at Oak Ridge National Laboratory, USA. For the hexagonal close-packed (*hcp*) phase, strong nuclear and magnetic satellite intensities permit a simultaneous refinement of the nuclear and magnetic structures. At 1 GPa of applied pressure, a modulation vector $\boldsymbol{q} = \gamma \boldsymbol{c}^*$ with $\gamma \approx 2/7$ for the *c*-axis modulated and cycloidal phases is consistent with prior single-crystal studies at low pressures. At 6.7 GPa in the *hcp* phase, we find $\gamma \approx 0.31$, indicating a reduction in the period of the magnetic structure with respect to the crystal lattice. The magnetic ordering temperature at 6.7 GPa is slightly above 60 K. At 32 GPa in the double hexagonal close-packed phase, the magnetic scattering constrains the magnetic ordering temperature to 25 ± 5 K. Our neutron diffraction study demonstrates that the magnetic ordering persists in the high-pressure double hexagonal close-packed phase of erbium to the highest pressure of 32 GPa.

1. INTRODUCTION

The lanthanides form a technologically important series of elements which are routinely exploited for their properties in permanent magnets, laser gain media and many other applications [1]. Upon cooling, many lanthanides magnetically order as highly localized 4*f* magnetic moments interact through polarized conduction electrons, as described by the Ruderman–Kittel–Kasuya–Yosida

interaction [2]. The vast number and complexity of magnetic structures exhibited by the lanthanides have been the focus of scientific inquiry for many decades [3,4]. Erbium in particular has been the subject of numerous investigations, and much remains to be explored, especially under the application of high pressure.

Single-crystal neutron diffraction studies have identified three magnetic phase transitions in the *hcp* phase of erbium as it is cooled at atmospheric pressure and under zero applied field [5]. Beginning at 80 K, the moments order parallel to the *c* axis of the hexagonal unit cell and are sinusoidally modulated with a modulation vector $\boldsymbol{q} \approx (2/7)\boldsymbol{c}^*$, in the so-called *c*-axis modulated (CAM) phase. Upon further cooling, higher-order harmonics appear and correspond to a squaring-up of the sinusoidal structure [6]. Below 52 K, satellites flanking (00L) nuclear reflections emerge and indicate ordering of moments with finite projections in the basal plane [5], and the resulting structure is cycloidal in the *a*-*c* plane [7]. Further cooling below the Curie point at 20 K produces a conical ferromagnetic structure, with the *c*-axis components ferromagnetically aligned and the basal plane components forming a spiral [3].

This general picture has been refined by numerous studies. From a combined x-ray and neutron scattering experiment, Gibbs et al. [8] observed a reduction in the magnitude of the modulation vector with decreasing temperature for the cycloidal phase and a series of lock-ins to rational wave vectors, i.e., commensurate magnetic structures. A similar temperature dependence of the modulation vector was observed by Lin et al. [9,10], who also found that applied fields along the *c* axis stabilized those commensurate structures in the cycloidal phase with a net ferrimagnetic moment. Jensen and Cowley [7] found that the cycloidal phase is not planar in the *a*-*c* plane, but in fact wobbles, with a small *b*-axis component of the moment. These x-ray and neutron scattering experiments have been complemented by magnetization [11–14], resistance [15–17], dilatometry

[18] and other experiments [19,20] to map out the rich phase diagram of erbium in the *H-T* plane.

While the magnetic properties of erbium have been studied extensively at ambient pressure, much less is known at high pressures. Early inductance measurements by Milton and Scott [21] up to 0.7 GPa found a reduction in all transition temperatures with applied pressure. The resistance measurements of Thomas et al. [22,23] also showed a reduction in the Néel point with increasing pressure, and a disappearance of the corresponding resistance anomaly at the transition between the hexagonal close-packed (*hcp*) and alpha-Samarium (*α-Sm*) phases. The resistance and neutron diffraction experiments of Ellerby et al. [24,25] showed that 0.5 GPa of applied pressure is sufficient to suppress the conical ferromagnetic phase at 6 K. The single crystal neutron diffraction studies of Kawano et al. at 1.15 GPa [26] and 1.4 GPa [27] also demonstrated a suppression of the conical phase, and a lock-in to a modulation vector $\boldsymbol{q} \approx (2/7)\boldsymbol{c}^*$ below 30 K in the cycloidal phase at 1.4 GPa. These structural studies are all at relatively low pressure and thus limited to the *hcp* phase of erbium. Data is lacking for the *hcp* phase at even higher pressures and the other structural phases erbium adopts with increasing pressure.

In this paper, we present a high-pressure neutron diffraction study on polycrystalline erbium. We focus on magnetic structure modeling in the *hcp* phase at 1 GPa and 6.7 GPa, and for the highest pressure of 32 GPa, where erbium is in the double hexagonal close-packed (*dhcp*) phase, magnetic scattering provides an estimate of the magnetic ordering temperature. In Section 2, we describe the experimental methods. In Section 3, we present and discuss our results. Finally, in Section 4 we summarize our conclusions from this work and discuss paths for future research.

2. METHODS

A 99.9% pure polycrystalline erbium foil of 100 microns thickness was used for the time-of-flight (TOF) neutron diffraction experiment at BL-3 (SNAP) of the Spallation Neutron Source at Oak Ridge National Laboratory, USA. Choppers enabled two-frame data collection at nominal

wavelengths 2.1 Å and 6.4 Å to cover a wide Q range. Data collection times were based on set values of accumulated proton charge hitting the mercury target. Most runs lasted either two hours (5.1 C of proton charge) for the *hcp* phase, or about six hours (15.3 C of proton charge) for the *dhcp* phase at 32 GPa. To improve statistics, both area detectors were positioned 0.5 m from the sample with $2\theta = 65^{\circ}$ relative to the incident beam. A diamond anvil cell (DAC) [28] with diamonds grown by chemical vapor deposition was used to apply pressure. The diamonds were 5 mm tall, 5 mm in diameter and had 1.5 mm culets. A 301 stainless steel gasket of initial thickness 250 microns was indented to 100 microns thickness, after which a 770-micron diameter hole was laser drilled to form the sample chamber. A disk of the sample was laser cut to fill the hole, and ruby powder was added to serve as a pressure marker. A boron nitride collimator with an inner diameter of 530 microns was affixed to the DAC upstream of the sample to collimate the incident neutron beam. Once installed at the beamline, the DAC was cooled by a closed cycle refrigerator down to 10 K. The data was reduced in Mantid [29] and analyzed with FullProf [30], and magnetic structures were visualized with FPStudio. The erbium foil was also characterized using an Empyrean X-ray diffractometer by Malvern Panalytical with a copper X-ray source, and the Vibrating Sample Magnetometer (VSM) module of a Physical Property Measurement System by Quantum Design.

3. RESULTS AND DISCUSSION

Characterization of the erbium foil using laboratory X-ray diffraction experiments indicated a strong texture, with the *c* axis preferentially aligned with the normal to the surface of the foil. A small sample (0.0035 g) was cut and placed in the VSM for magnetization measurements with the surface normal perpendicular to the direction of oscillation of the VSM. Following cooling of the sample to 2 K in zero field, an H = 100 Oe field was applied, and data collected during warming, cooling, and rewarming cycles. The resulting inverse magnetic susceptibility is shown in Fig. 1 as

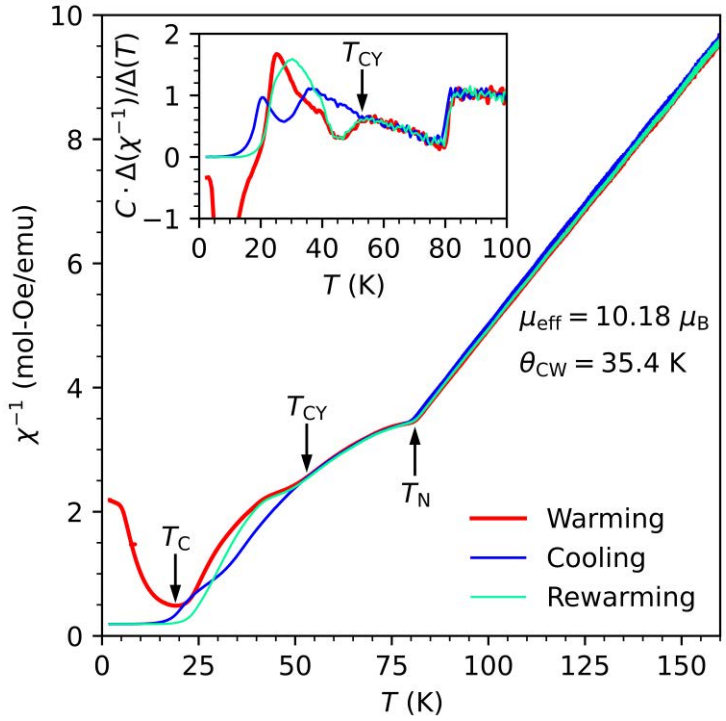

Fig. 1. Vibrating sample magnetometry results for erbium foil in an applied field of $H = 100$ Oe. Data taken during (red) warming, (blue) cooling, and (cyan) rewarming cycles between temperatures of 2 and 160 K at pressures ranging between 0.3 and 3.5 Torr. The heating and cooling rate was set to 0.25 K/min. Temperatures of magnetic transitions were estimated using the normalized slope (see inset) computed with central finite differences with 300 evenly spaced sample points from each cycle (finite difference results are robust with this sample count). The Néel point is $T_N = 81 \pm 1$ K, the transition from the sinusoidal phase to the cycloidal phase occurs at $T_{CY} = 53 \pm 1$ K and the Curie point is $T_C = 19 \pm 1$ K. Errors estimated from discrepancy between cooling and warming data in the paramagnetic regime, which arises from a lag between sample and chamber temperatures.

a function of temperature. The inverse magnetic susceptibility in the paramagnetic regime was fit to the Curie-Weiss law $\chi^{-1} = (T - \Theta_{CW})/C$, giving an effective moment $\mu_{\text{eff}} = \sqrt{8C}\,\mu_B = 10.18\,\mu_B$ and $\Theta_{CW} = 35.4$ K. The value of the moment can be compared to the theoretical value of 9.6 μ_B for Er^{3+} in the ground state $^4I_{15/2}$. We observed that in the CAM phase ($T_{CY} < T < T_N$), the heating and cooling curves agree well, but in the cycloidal phase ($T_C < T < T_{CY}$), there is considerable hysteresis. To help identify the transition temperatures, we down sampled the VSM data and differentiated them with a finite difference, the result of which is shown in the inset. The transition between the CAM and cycloidal phases is marked by a change in slope of the inverse susceptibility and is denoted by T_{CY}. The transition temperatures $T_N = 81 \pm 1$ K, $T_{CY} = 53 \pm 1$ K

and $T_C = 19 \pm 1$ K are in excellent agreement with the established values in the literature [5].

The first neutron diffraction data were collected following compression to 1 GPa. Data were collected at 290, 100, 80, 60, 40, 20 and 10 K during the cooling cycle. The spectra for 80 K and below are plotted in Fig. 2. The nuclear spectrum at 80 K clearly shows the heavy texturing of the foil: the (002) nuclear reflection is completely absent. As mentioned previously, the hallmark of the cycloidal phase is the presence of magnetic satellites flanking (00L) nuclear reflections, and single-crystal neutron diffraction studies typically focus on (002) [5,10]. Because we do not observe the (002) nuclear reflection nor its satellites, we cannot make an unambiguous identification of T_{CY}. Upon cooling below 80 K, the sample magnetically orders, and magnetic satellite reflections grow in intensity with reducing temperature. While we cannot discern the (102) nuclear reflection due to strong diamond (111) contamination in the spectra, we clearly see its first-order satellite reflections at low temperatures. Despite the relatively high intensity of the magnetic satellite reflections, we do not observe higher-order harmonics in the spectra. We also do not observe any reflections originating from the sample for lower values of Q than shown in Fig. 2. Finally, there is no evidence of ferromagnetism in the spectra, indicating that the conical phase is suppressed at 10 K.

In Fig. 2, we also present the results of Rietveld refinement analysis conducted with FullProf [30]. The modified March texture model with a preferred direction $\boldsymbol{d}^*_{101}$ in reciprocal space captures the texturing well. For magnetic structure refinements, both the nuclear structure and modulation vector $\boldsymbol{q} = \gamma \boldsymbol{c}^*$ were refined simultaneously. Basis vectors for the magnetic moments of CAM and cycloidal models were generated with SARAh [31,32] and used for the magnetic structure refinements. The space group for the *hcp* phase used to construct the models is $P6_3/mmc$, and the two erbium atoms have fractional coordinates (1/3, 2/3, 1/4) and (2/3, 1/3, 3/4) in the

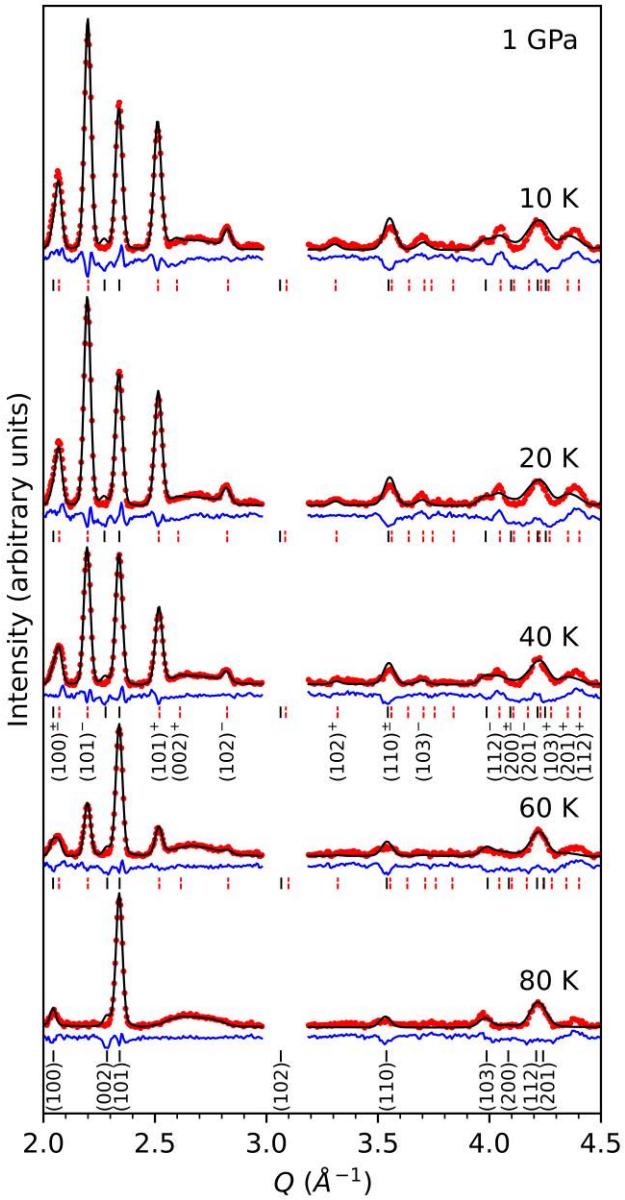

Fig. 2. Neutron diffraction data (red circles), results from Rietveld refinement (black curves) and their difference (blue curves) for erbium at 1 GPa. Spectra taken while cooling. Bragg positions for nuclear reflections marked with solid black lines, and Miller indices for the *hcp* nuclear structure labeled below the 80 K spectrum. Bragg positions for magnetic satellite reflections generated using the $P\bar{1}$ space group marked with dashed red lines. Select satellite reflections are labeled according to their neighboring nuclear reflection and superscript $+$ or $-$ to indicate addition or subtraction of the modulation vector $\boldsymbol{q}$ in reciprocal space, respectively. For example, $\boldsymbol{d}^*_{101} - \boldsymbol{q}$ is denoted by $(101)^-$. Data in the range $2.98\ \text{Å}^{-1} \leq Q \leq 3.18\ \text{Å}^{-1}$ are omitted from the analysis due to a strong diamond (111) reflection.

hexagonal unit cell. The basis vector for the magnetic moment of the first atom in the CAM model in the crystallographic coordinate system is simply (0, 0, 1). For the cycloidal model, after taking suitable linear combinations of the basis vectors generated by SARAh, the first atom has basis

Table 1. Rietveld refinement results for erbium upon cooling at a pressure of 1 GPa in the *hcp* phase. The modulation vector for the magnetically ordered phase is $\boldsymbol{q} = \gamma \boldsymbol{c}^*$, where $\boldsymbol{c}^*$ is the reciprocal lattice vector that is parallel to the *c* axis. The sample is magnetically ordered at 60 K, where a *c*-axis modulated (CAM) sinusoidal model for the moments is applied. For 40 K and below, a cycloidal model in the *a*-*c* plane is used. No harmonics are included in these models. The components of the magnetic moment along the *c* and *a* axes are μ_c and μ_a, respectively, and μ_B is the Bohr magneton. Quoted uncertainties are the estimated standard deviations provided by FullProf.

T (K)	a (Å)	c (Å)	γ	$\mu_{c,\max}/\mu_B$	$\mu_{a,\max}/\mu_B$	R_{Bragg}	R_{Mag}	χ^2
290	3.563(1)	5.539(5)	—	—	—	16.6	—	1.37
100	3.554(1)	5.507(5)	—	—	—	13.1	—	1.38
80	3.557(1)	5.511(5)	—	—	—	14.0	—	1.35
60	3.550(1)	5.496(4)	0.2890(10)	4.6(1)	—	7.32	19.0	1.19
40	3.540(1)	5.501(3)	0.2922(6)	6.6(3)	4.0(4)	6.66	8.11	1.29
20	3.535(1)	5.507(3)	0.2897(6)	8.3(3)	4.4(6)	9.20	8.30	2.19
10	3.534(1)	5.505(3)	0.2847(6)	7.8(3)	5.6(5)	9.58	9.06	2.77

vectors (i, 0, 0) and (0, 0, 1), with separate coefficients during refinement. For both models, the basis vectors for the second atom are obtained by multiplying those for the first atom by the phase factor $e^{-i\pi\gamma}$. FullProf ensures the magnetic moments are real by including contributions from the modulation vector $\boldsymbol{q} = -\gamma \boldsymbol{c}^*$ with the complex conjugates of the aforementioned basis vectors.

Following the reported value of $T_{\text{CY}} = 50$ K at 1.15 GPa by Kawano et al. [26], for our data at 1 GPa in Fig. 2, we used a CAM model for the 60 K datapoint and cycloidal models for the lower temperatures, both without any higher-order harmonics. The combined models are able to account for the nuclear intensities, magnetic satellite intensities and heavy texturing of the sample simultaneously. In Table 1, we summarize the results of the analysis. While the *a* lattice parameter decreases nearly monotonically with reducing temperature, the uncertainties in the *c* lattice parameter are too high to make definitive conclusions. At the lowest temperature of 10 K, the modulation vector is close to $\boldsymbol{q} = (2/7)\boldsymbol{c}^* \approx 0.2857\boldsymbol{c}^*$. The overall magnitude of the moments at low temperatures are in good agreement with prior models fit to single-crystal neutron diffraction data, e.g., see Table 3 in Kawano et al. [26]. In Fig. 3, we provide renderings of the CAM structure at 60 K and the cycloidal structure at 10 K. The period of each magnetic structure relative to the nuclear unit cell in the $\boldsymbol{c}$ direction is given by $1/\gamma$. For the cycloidal structure at 10 K, $1/\gamma \approx 3.51$, as is clear from the moment nearly completing a full rotation after moving up seven close-packed

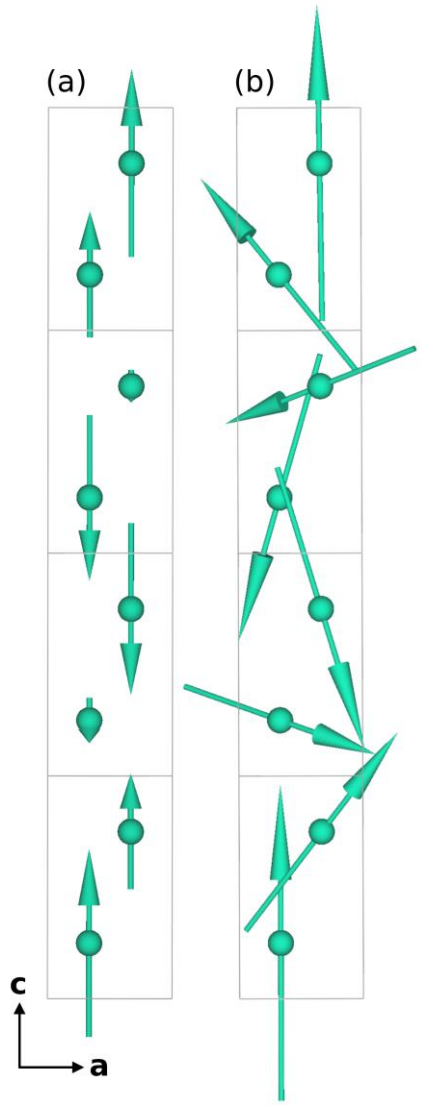

Fig. 3. Magnetic structures for erbium in the *hcp* phase at 1 GPa visualized in the *a*-*c* plane: (a) the CAM structure at 60 K and (b) the cycloidal structure at 10 K. See Table 1 for the sizes of the moments and the period of the magnetic structure relative to the nuclear unit cell $1/\gamma$.

layers in the *hcp* structure.

In Fig. 4 and Table 2, we present experimental data and Rietveld refinement results for erbium in the *hcp* phase at 6.7 GPa. The satellite $\boldsymbol{d}^*_{101} - \boldsymbol{q}$ is weakly present at 60 K, indicating that the magnetic ordering temperature is slightly above 60 K, which is consistent with previous resistance measurements at high pressure [22]. At 60 K, we fit a CAM model to the data. The very weak magnetic intensities at 60 K are reflected in a relatively large uncertainty in the refined modulation vector compared to the other datapoints, as seen in Table 2. Although we cannot identify T_{CY} with

Table 2. Rietveld refinement results for erbium upon cooling at a pressure of 6.7 GPa in the *hcp* phase. Data taken during the cooling cycle. The sample magnetically orders just above 60 K. At 60 K, a *c*-axis modulated (CAM) sinusoidal model for the moments is used, while for 40 K and below, a cycloidal model in the *a*-*c* plane is used. See caption of Table 1 for additional description.

T (K)	a (Å)	c (Å)	γ	$\mu_{c,\max}/\mu_B$	$\mu_{a,\max}/\mu_B$	R_{Bragg}	R_{Mag}	χ^2
200	3.443(1)	5.353(5)	—	—	—	15.3	—	1.10
80	3.443(1)	5.314(5)	—	—	—	15.0	—	1.14
60	3.443(1)	5.313(5)	0.3045(52)	2.1(2)	—	12.1	38.7	1.29
40	3.446(1)	5.319(4)	0.3144(8)	6.6(3)	3.3(6)	6.26	13.0	1.50
20	3.438(1)	5.319(4)	0.3132(8)	7.5(3)	5.3(5)	7.02	10.6	2.19
10	3.440(1)	5.329(4)	0.3106(8)	8.0(3)	5.4(5)	10.1	10.8	2.35

our data (see discussion above), we fit cycloidal models to the lower temperature data, and they reproduce the experimental spectra well. Referencing Table 2, we see that the modulation vector has departed from the $\gamma \approx 2/7$ behavior seen at lower pressures and now has $\gamma \approx 0.31$, indicating a reduction in the wavelength of the magnetic structure relative to the crystal lattice. Additional high-pressure data for the *hcp* phase would be useful to determine the pressure dependence of γ and to see if it approaches $\gamma = 1/3$. We also note that the conical phase is suppressed for these conditions.

Following data collection at 6.7 GPa, we further compressed the sample to 32 GPa, where erbium adopts the *dhcp* phase [33]. Here, data collected on warming showed evidence of the disappearance of scattering, consistent with a strong magnetic reflection at $Q \approx 2.33$ Å near the nuclear (100) reflection, as shown in Fig. 5. To confirm this observation, the sample was subsequently cooled, whereupon the signal reappeared. This confirms that erbium in the *dhcp* phase undergoes magnetic ordering, with a constraint in the magnetic ordering temperature of approximately 25 ± 5 K at 32 GPa. The temperatures used in this portion of the study were, in order: 10, 20, 40, 60, 80, 30 and 15 K. Despite long collection times, the scattering under these conditions was too weak to clearly identify the nuclear structure in the spectra.

4. CONCLUSIONS

In this paper, we have reported a high-pressure neutron diffraction study on polycrystalline erbium.

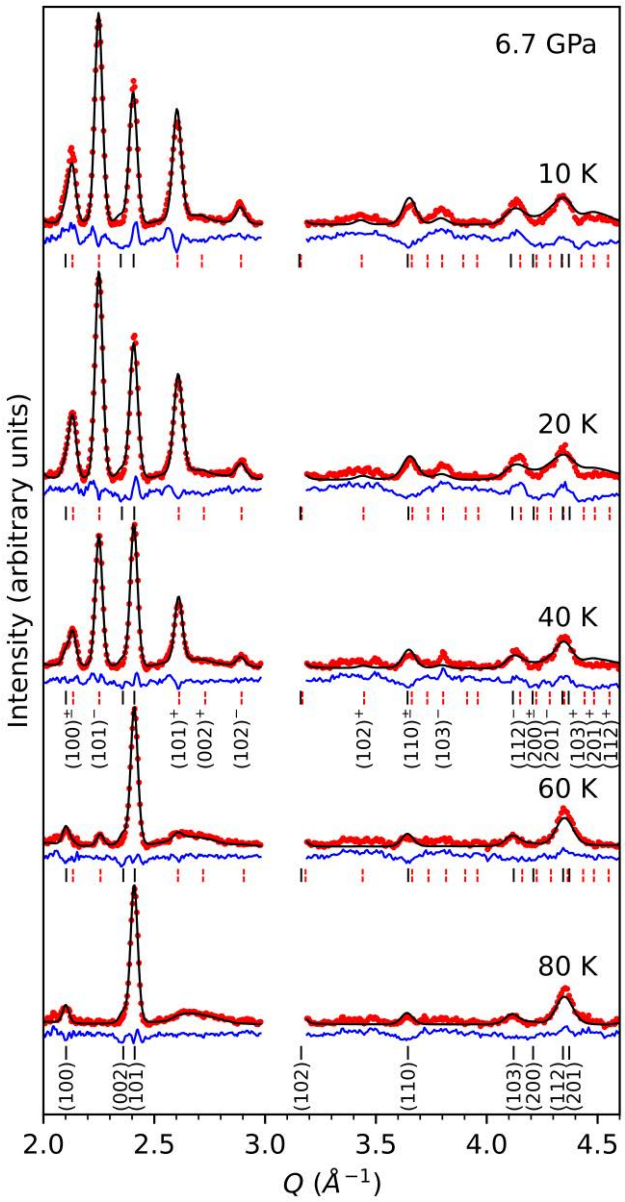

Fig. 4. Neutron diffraction data (red circles) and results from Rietveld refinement (black curves) for erbium at 6.7 GPa and various temperatures. See caption of Fig. 2 for additional description.

Our findings for the *hcp* phase at 1 GPa are consistent with prior single-crystal studies [26,27], which showed the adoption of *c*-axis modulated (CAM) and cycloidal magnetic structures with decreasing temperature, and a suppression of the conical ferromagnetic phase. Following magnetic ordering at 1 GPa, our data are well described by these structures, and, despite heavy texturing of the foil sample, Rietveld refinements with FullProf successfully capture the nuclear and magnetic

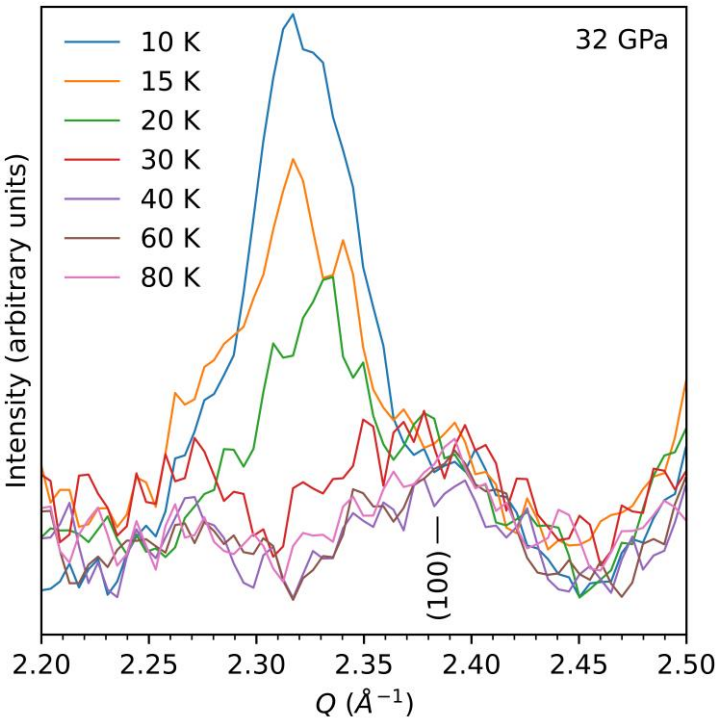

Fig. 5. Neutron diffraction data for erbium at 32 GPa. Data collected in the following order: 10, 20, 40, 60, 80, 30 and 15 K. Location of (100) nuclear Bragg reflection computed with lattice parameters of erbium at 32 GPa as determined by the X-ray diffraction experiments of Samudrala et al. [33].

components of the spectra. Following compression to 6.7 GPa, where erbium is still in the *hcp* phase, we observe a change in the modulation vector from the $\boldsymbol{q} = (2/7)\boldsymbol{c}^* \approx 0.2857\boldsymbol{c}^*$ behavior seen at low pressures to $\boldsymbol{q} \approx 0.31\boldsymbol{c}^*$, indicating a reduction in the period of the magnetic structure relative to the crystal lattice. Our data at 6.7 GPa also show that the magnetic ordering temperature is near 60 K, which is consistent with high-pressure electrical resistance experiments [22]. Following compression to 32 GPa, where erbium adopts the *dhcp* phase, the temperature dependence of a strong magnetic reflection in the data near the (100) nuclear reflection allows us to conclude that the magnetic ordering temperature is 25 ± 5 K. Additional experiments in the *hcp* phase would help to establish the pressure dependence of the modulation vector $\boldsymbol{q} = \gamma\boldsymbol{c}^*$, and, if sample texturing can be avoided, the transition temperature between the CAM and cycloidal phases T_{CY}. Our studies also demonstrate that magnetic ordering persists in the high-pressure *dhcp* phase of erbium at the highest pressure of 32 GPa reached in the neutron diffraction experiment.

DECLARATION OF COMPETING INTEREST

The authors declare that they have no known competing financial interests or personal relationships that could have appeared to influence the work reported in this paper.

DATA AVAILABILITY

Data will be made available on reasonable request.

ACKNOWLEDGEMENTS

This material is based upon work supported by the Department of Energy-Basic Energy Sciences under Award Number DE-SC0023268. The Physical Properties Measurements System (PPMS) employed in this study was acquired under NSF MRI Grant No. 2215143. This research used resources at the Spallation Neutron Source, a DOE Office of Science User Facility operated by the Oak Ridge National Laboratory. Maurissa Higgins acknowledges support from the NSF Research Experiences for Undergraduates (REU)-site under Award Number DMR-2148897. Matthew Clay would like to thank Dr. S. A. Calder for his helpful suggestions about conducting magnetic structure refinements with FullProf.

REFERENCES

[1] J. Zhou, G.A. Fiete, Rare earths in a nutshell, Phys. Today 73 (2020) 66–67. https://doi.org/10.1063/PT.3.4397.

[2] J. Jensen, A.R. Mackintosh, Rare earth magnetism: structures and excitations, Clarendon Press ; Oxford University Press, Oxford : New York, 1991.

[3] W.C. Koehler, Magnetic Properties of Rare-Earth Metals and Alloys, J. Appl. Phys. 36 (1965) 1078–1087. https://doi.org/10.1063/1.1714108.

[4] R. Gimaev, A. Komlev, A. Davydov, B. Kovalev, V. Zverev, Magnetic and Electronic Properties of Heavy Lanthanides (Gd, Tb, Dy, Er, Ho, Tm), Crystals 11 (2021) 82. https://doi.org/10.3390/cryst11020082.

[5] J.W. Cable, E.O. Wollan, W.C. Koehler, M.K. Wilkinson, Magnetic Structures of Metallic Erbium, Phys. Rev. 140 (1965) A1896–A1902. https://doi.org/10.1103/PhysRev.140.A1896.

[6] M. Habenschuss, C. Stassis, S.K. Sinha, H.W. Deckman, F.H. Spedding, Neutron diffraction study of the magnetic structure of erbium, Phys. Rev. B 10 (1974) 1020–1026.

https://doi.org/10.1103/PhysRevB.10.1020.

[7] J. Jensen, R.A. Cowley, Non-Planar Magnetic Structures and Trigonal Interactions in Erbium, Europhys. Lett. 21 (1993) 705. https://doi.org/10.1209/0295-5075/21/6/012.

[8] D. Gibbs, J. Bohr, J.D. Axe, D.E. Moncton, K.L. D'Amico, Magnetic structure of erbium, Phys. Rev. B 34 (1986) 8182–8185. https://doi.org/10.1103/PhysRevB.34.8182.

[9] H. Lin, M.F. Collins, T.M. Holden, W. Wei, Magnetic structure of erbium in field, J. Magn. Magn. Mater. 104–107 (1992) 1511–1512. https://doi.org/10.1016/0304-8853(92)91431-R.

[10] H. Lin, M.F. Collins, T.M. Holden, W. Wei, Magnetic structure of erbium, Phys. Rev. B 45 (1992) 12873–12882. https://doi.org/10.1103/PhysRevB.45.12873.

[11] R.W. Green, S. Legvold, F.H. Spedding, Magnetization and Electrical Resistivity of Erbium Single Crystals, Phys. Rev. 122 (1961) 827–830. https://doi.org/10.1103/PhysRev.122.827.

[12] S. Gama, M.E. Fóglio, Magnetization of erbium in the ordered and paramagnetic phases, Phys. Rev. B 37 (1988) 2123–2132. https://doi.org/10.1103/PhysRevB.37.2123.

[13] H.U. Astrom, D.-X. Chen, G. Benediktsson, K.V. Rao, Low-field AC susceptibility measurements on monocrystalline erbium, J. Phys. Condens. Matter 2 (1990) 3349. https://doi.org/10.1088/0953-8984/2/14/019.

[14] N. Ali, F. Willis, Magnetization of single-crystal erbium, Phys. Rev. B 42 (1990) 6820–6822. https://doi.org/10.1103/PhysRevB.42.6820.

[15] F. Willis, N. Ali, Effect of spin slip structures on the resistivity of erbium and holmium, J. Alloys Compd. 181 (1992) 287–292. https://doi.org/10.1016/0925-8388(92)90324-3.

[16] B. Watson, N. Ali, Magnetic transitions in single-crystal erbium, J. Phys. Condens. Matter 7 (1995) 4713–4723. https://doi.org/10.1088/0953-8984/7/24/011.

[17] B. Watson, N. Ali, On the phase diagram of erbium, J. Alloys Compd. 250 (1997) 662–665. https://doi.org/10.1016/S0925-8388(96)03040-X.

[18] S.W. Zochowski, K.A. McEwen, Dilatometric study of the magnetic phase diagram of erbium, J. Magn. Magn. Mater. 140–144 (1995) 1127–1128. https://doi.org/10.1016/0304-8853(94)00764-0.

[19] H.U. Astrom, G. Benediktsson, On magnetic first-order transitions in erbium, J. Phys. Condens. Matter 1 (1989) 4381. https://doi.org/10.1088/0953-8984/1/27/010.

[20] R.S. Eccleston, S.B. Palmer, Magnetoelastic effects in single-crystal erbium, J. Phys. Condens. Matter 4 (1992) 10037. https://doi.org/10.1088/0953-8984/4/49/030.

[21] J.E. Milton, T.A. Scott, Pressure Dependence of the Magnetic Transitions in Dysprosium

and Erbium, Phys. Rev. 160 (1967) 387–392. https://doi.org/10.1103/PhysRev.160.387.

[22] S.A. Thomas, G.M. Tsoi, L.E. Wenger, Y.K. Vohra, S.T. Weir, Magnetic and structural phase transitions in erbium at low temperatures and high pressures, Phys. Rev. B 84 (2011) 144415. https://doi.org/10.1103/PhysRevB.84.144415.

[23] S.A. Thomas, G.M. Tsoi, L.E. Wenger, Y.K. Vohra, S.T. Weir, Magnetic transitions in erbium at high pressures, J. Appl. Phys. 111 (2012) 07E104. https://doi.org/10.1063/1.3670970.

[24] M. Ellerby, K.A. McEwen, E. Bauer, R. Hauser, J. Jensen, Pressure-dependent resistivity and magnetoresistivity of erbium, Phys. Rev. B 61 (2000) 6790–6797. https://doi.org/10.1103/PhysRevB.61.6790.

[25] M. Ellerby, K.A. Mcewen, J. Jensen, M.J. Bull, Neutron Diffraction Study of the p - T Phase Diagram for Erbium, High Press. Res. 22 (2002) 369–373. https://doi.org/10.1080/08957950212812.

[26] S. Kawano, B. Lebech, N. Achiwa, Magnetic structures of erbium under high pressure, J. Phys. Condens. Matter 5 (1993) 1535–1546. https://doi.org/10.1088/0953-8984/5/10/011.

[27] S. Kawano, S.Aa. Sørensen, B. Lebech, N. Achiwa, High pressure neutron diffraction studies of the magnetic structures of erbium, J. Magn. Magn. Mater. 140–144 (1995) 763–764. https://doi.org/10.1016/0304-8853(94)00756-X.

[28] B. Haberl, M. Guthrie, R. Boehler, Advancing neutron diffraction for accurate structural measurement of light elements at megabar pressures, Sci. Rep. 13 (2023) 4741. https://doi.org/10.1038/s41598-023-31295-3.

[29] O. Arnold, J.C. Bilheux, J.M. Borreguero, A. Buts, S.I. Campbell, L. Chapon, M. Doucet, N. Draper, R. Ferraz Leal, M.A. Gigg, V.E. Lynch, A. Markvardsen, D.J. Mikkelson, R.L. Mikkelson, R. Miller, K. Palmen, P. Parker, G. Passos, T.G. Perring, P.F. Peterson, S. Ren, M.A. Reuter, A.T. Savici, J.W. Taylor, R.J. Taylor, R. Tolchenov, W. Zhou, J. Zikovsky, Mantid—Data analysis and visualization package for neutron scattering and μ SR experiments, Nucl. Instrum. Methods Phys. Res. Sect. Accel. Spectrometers Detect. Assoc. Equip. 764 (2014) 156–166. https://doi.org/10.1016/j.nima.2014.07.029.

[30] J. Rodríguez-Carvajal, Recent advances in magnetic structure determination by neutron powder diffraction, Phys. B Condens. Matter 192 (1993) 55–69. https://doi.org/10.1016/0921-4526(93)90108-I.

[31] A.S. Wills, A new protocol for the determination of magnetic structures using simulated annealing and representational analysis (SARAh), Phys. B Condens. Matter 276–278 (2000) 680–681. https://doi.org/10.1016/S0921-4526(99)01722-6.

[32] A. Wills, Magnetic structures and their determination using group theory, J. Phys. IV 11 (2001) Pr9-133-Pr9-158. https://doi.org/10.1051/jp4:2001906.

[33] G.K. Samudrala, Y.K. Vohra, Structural Properties of Lanthanides at Ultra High Pressure, in: Handb. Phys. Chem. Rare Earths, Elsevier, 2013: pp. 275–319. https://doi.org/10.1016/B978-0-444-59536-2.00004-0.